



HAL
open science

Morphological profiling of T cells predicts clinical response to VLA-4-targeting natalizumab therapy in patients with multiple sclerosis

Beatriz Chaves, Juan Carlo Santos E Silva, Helder Nakaya, Matheus Almeida, Florence Bucciarelli, Claire Lacouture, Guilhèn Prunier, Saniya Kari, Anne Laurence Astier, Marco Medeiros, et al.

► To cite this version:

Beatriz Chaves, Juan Carlo Santos E Silva, Helder Nakaya, Matheus Almeida, Florence Bucciarelli, et al.. Morphological profiling of T cells predicts clinical response to VLA-4-targeting natalizumab therapy in patients with multiple sclerosis. 2024. inserm-04728349

HAL Id: inserm-04728349

<https://inserm.hal.science/inserm-04728349v1>

Preprint submitted on 9 Oct 2024

HAL is a multi-disciplinary open access archive for the deposit and dissemination of scientific research documents, whether they are published or not. The documents may come from teaching and research institutions in France or abroad, or from public or private research centers.

L'archive ouverte pluridisciplinaire **HAL**, est destinée au dépôt et à la diffusion de documents scientifiques de niveau recherche, publiés ou non, émanant des établissements d'enseignement et de recherche français ou étrangers, des laboratoires publics ou privés.



Distributed under a Creative Commons Attribution 4.0 International License

Morphological profiling of T cells predicts clinical response to VLA-4-targeting natalizumab therapy in patients with multiple sclerosis

Beatriz Chaves

`beatriz.chaves@inserm.fr`

INSERM

Juan Carlo Santos e Silva

USP <https://orcid.org/0000-0002-7327-4294>

Helder Nakaya

University of Sao Paulo <https://orcid.org/0000-0001-5297-9108>

Matheus Almeida

Fundação Oswaldo Cruz (Fiocruz)

Florence Bucciarelli

University of Toulouse

Claire Lacouture

Toulouse Institute for Infectious and Inflammatory Diseases (INFINITY)

Guilhèn Prunier

Toulouse Institute for Infectious and Inflammatory Diseases (INFINITY)

Saniya Kari

Toulouse Institute for Infectious and Inflammatory Diseases (INFINITY) <https://orcid.org/0009-0002-5392-0428>

Anne Astier

INSERM U1043 <https://orcid.org/0000-0002-0144-3431>

Marco Medeiros

Instituto de Tecnologia em Imunobiológicos (Bio-Manguinhos)

João Hermínio da Silva

Fundação Oswaldo Cruz (Fiocruz)

Roland Liblau

Institut National de la Santé et de la Recherche Médicale Unit 563, Purpan University Hospital
<https://orcid.org/0000-0001-5477-5475>

Vinícius Cotta-de-Almeida

Instituto Oswaldo Cruz (IOC)

Loïc Dupré

INSERM, UMR1291, Toulouse Institute for Infectious and Inflammatory Diseases, Toulouse
<https://orcid.org/0000-0002-7278-6503>

Article

Keywords: Multiple sclerosis, T cells, VLA-4, natalizumab, high-content cell imaging, pretreatment testing of drug efficacy

Posted Date: June 12th, 2024

DOI: <https://doi.org/10.21203/rs.3.rs-4536459/v1>

License: © ⓘ This work is licensed under a Creative Commons Attribution 4.0 International License.
[Read Full License](#)

Additional Declarations: There is **NO** Competing Interest.

1 **Morphological profiling of T cells predicts clinical response to VLA-4-**
2 **targeting natalizumab therapy in patients with multiple sclerosis**

3
4 Beatriz Chaves^{1,2,3}, Juan Carlo Santos e Silva⁴, Helder Nakaya⁵, Matheus V. Almeida²,
5 Florence Bucciarelli^{1,6}, Claire Lacouture¹, Guilhèn Prunier¹, Saniya Kari¹, Anne L. Astier¹,
6 Marco A. Medeiros⁷, João H.M Silva^{2,3}, Roland Liblau^{1,8}, Vinicius Cotta-de-Almeida^{3,9,10*} and
7 Loïc Dupré^{1,11*}

8
9 ¹ Toulouse Institute for Infectious and Inflammatory Diseases (INFINITY), INSERM U1291,
10 CNRS UMR5051, Toulouse III Paul Sabatier University, Toulouse, France.

11 ² Structural and Functional Biology of Biopharmaceuticals, Fiocruz-Ceará, Oswaldo Cruz
12 Foundation (Fiocruz), Eusébio, Brazil.

13 ³ National Institute of Science and Technology on Neuroimmunomodulation (INCT-NIM),
14 Oswaldo Cruz Institute, Oswaldo Cruz Foundation (Fiocruz), Rio de Janeiro, Brazil.

15 ⁴ Department of Clinical and Toxicological Analyses, School of Pharmaceutical Sciences,
16 University of São Paulo, São Paulo, Brazil.

17 ⁵ Hospital Israelita Albert Einstein, São Paulo, Brazil.

18 ⁶ Department of Neurosciences, Toulouse University Hospitals, Toulouse, France.

19 ⁷ Laboratory of Recombinant Technology, Bio-Manguinhos, Oswaldo Cruz Foundation
20 (Fiocruz), Rio de Janeiro, Brazil.

21 ⁸ Department of Immunology, Toulouse University Hospitals, Toulouse, France.

22 ⁹ Laboratory on Thymus Research (LPT), Oswaldo Cruz Institute (IOC), Oswaldo Cruz
23 Foundation (Fiocruz), Rio de Janeiro, Brazil.

24 ¹⁰ Rio de Janeiro Research Network on Neuroinflammation (RENEURIN), Oswaldo Cruz
25 Institute, Oswaldo Cruz Foundation (Fiocruz), Rio de Janeiro, Brazil.

26 ¹¹ Department of Dermatology, Medical University of Vienna, Vienna, Austria.

27
28 * Equal contribution to the work

29
30 Corresponding authors and lead contacts:

31 Loïc Dupré, Toulouse Institute for Infectious and Inflammatory Diseases, Toulouse, France. E-
32 mail: loic.dupre@inserm.fr

33 Vinicius Cotta-de-Almeida, Oswaldo Cruz Institute, Laboratory on Thymus Research, Oswaldo
34 Cruz Foundation, Rio de Janeiro, Brazil. E-mail: vinicius.almeida@fiocruz.br

35

36 **Abstract**

37 Despite the efficacy of natalizumab in Multiple Sclerosis (MS) treatment, approximately 30%
38 of patients do not respond favorably. Individual heterogeneity of T-cell response to VLA-4
39 natalizumab-mediated blockade may underlie disparities in treatment efficacy. Here, a high-
40 content cell imaging (HCI) pipeline was implemented to profile the *in vitro* effects of
41 natalizumab on VLA-4-stimulated leukocytes from MS patients prior to treatment.
42 Unsupervised clustering of image data partially discriminated non-responder MS patients based
43 on morphology, F-actin organization, and signaling-related features in CD8⁺ T cells. Treatment
44 response was assessed through a Random Forest approach with predictive performance of 91%
45 for a discovery cohort and 70% for a validation cohort. Unfavorable treatment response was
46 associated with the inefficacy of natalizumab to impair the ability of pretreated CD8⁺ T cells to
47 spread over VCAM-1. Our study unveils that CD8⁺ T cells from individual MS patients display
48 heterogeneous susceptibility to natalizumab *in vitro* and highlights the potential of HCI-based
49 pretreatment monitoring to assist individualized treatment prescription.

50

51 **Keywords**

52 Multiple sclerosis; T cells; VLA-4; natalizumab; high-content cell imaging; pretreatment
53 testing of drug efficacy

54 Introduction

55 Very Late Antigen-4 (VLA-4) is a heterodimeric integrin composed by the $\alpha 4$ and $\beta 1$ subunits
56 ¹. VLA-4 mediates adhesion, transmigration and intra-tissue trafficking of immune cells,
57 including T cells, by interacting with Vascular Cell Adhesion Molecule-1 (VCAM-1) and
58 fibronectin ². In addition, this integrin is involved in T-cell immune synapse (IS) assembly ³
59 and activation ^{4,5}. Because of its pivotal role in multiple aspects of T-cell biology, VLA-4 also
60 contributes to mediate dysregulated T-cell responses, such as those underlying inflammatory
61 diseases ⁶. This integrin has been particularly studied in the context of multiple sclerosis (MS),
62 in which lymphocytes overexpress VLA-4 on their surface ⁷ facilitating transmigration to the
63 central nervous system (CNS) ⁸⁻¹⁰. The identification of this mechanism has been the rationale
64 for targeting VLA-4 as a therapeutic approach to treat MS ^{11,12}.

65 The humanized anti- $\alpha 4$ monoclonal antibody natalizumab, which blocks VLA-4-VCAM-1
66 interaction, is currently used to treat relapsing-remitting MS (RRMS) patients ^{13,14} This
67 therapeutic antibody acts primarily by reducing the homing of pathogenic lymphocytes and
68 activated monocytes to the CNS ¹⁵. The NEDA end point (no evidence of disease activity) is
69 commonly used to define controlled MS ¹⁶. Currently, 30% of RRMS patients treated with
70 natalizumab present evidence of disease activity ¹⁷, not satisfactorily responding to the
71 treatment according to the NEDA criteria. VLA-4 expression on Peripheral Blood Mononuclear
72 Cells (PBMCs) ¹⁸, serum levels of IgM specific for phosphatidylcholine ¹⁹, metalloproteinases
73 ²⁰, low percentage of CD5⁺ B cells ²¹, age at prescription and disease duration ²² have been
74 pointed as biological parameters related to natalizumab clinical response, although their
75 robustness as predictive biomarkers remains to be established. To date, we therefore lack a
76 pretreatment test to predict whether a given person with MS might benefit from the therapy.
77 This would be particularly relevant to avoid exposing unresponsive patients to potential risks,
78 such as the JC virus-associated Progressive Multifocal Leukoencephalopathy (PML) ²³, and to
79 tailor treatment decision toward other available therapeutic lines. In this context, we reasoned
80 that profiling the *in vitro* response to natalizumab of leukocytes from MS patients might predict
81 treatment response and therefore assist treatment decision.

82 For this purpose, we opted for a high-content cell imaging (HCI) approach to monitor the *in*
83 *vitro* effect of natalizumab on PBMCs from persons with MS prior to treatment. This approach
84 allows to extract precise morphological and molecular metrics pertaining to leukocyte adhesion
85 ²⁴. Because of its deep phenotyping power, it is also particularly prone to discriminate subtle

86 donor-specific traits that may relate to individual health status²⁵ and responsiveness to therapies
87 ²⁶. We first implemented the approach on healthy donor PBMCs and then applied it to MS
88 patients' PBMCs, which pointed to CD8⁺ T cells as the cellular subset for which the most
89 pronounced impact of natalizumab exposure could be captured, based on descriptors related to
90 morphology, F-actin and phospho-SLP76. Unsupervised analysis of the HCI data yielded 2 MS
91 patient subgroups with distinct CD8⁺ T-cell responses that partially aligned with the subsequent
92 treatment response. A machine-learning based approach using the features from the image
93 dataset of a discovery cohort and applied to a validation cohort highlighted the predictive power
94 of the herein developed pre-treatment morphological profiling approach.

95 **Results**

96 **High-content cell imaging captures the *in vitro* sensitivity of primary T cells to** 97 **natalizumab**

98 Key molecular events underlying the ability of VLA-4 to trigger leukocyte adhesion, spreading
99 and activation are the recruitment of the adaptor protein SLP76 and the remodeling of the actin
100 cytoskeleton^{4,27,28}. Therefore, to profile the *ex vivo* response of T cells to natalizumab, we
101 implemented an HCI approach, which offered the possibility to collect concomitantly features
102 pertaining to cell morphology, SLP76 phosphorylation and F-actin organization. The HCI
103 pipeline was first optimized on frozen PBMC samples from 10 HD that were or not exposed *in*
104 *vitro* to natalizumab and seeded onto VCAM-1-coated 384-well imaging plates for analyzing
105 T-cell subsets based on a staining for the CD4 and CD8 coreceptors. Automated confocal
106 imaging was conducted with a 40X objective by focusing on the ventral side of the cells where
107 they were interacting with the VCAM-1-coated surface. A set of 5 descriptors was selected *a*
108 *priori* for the analysis, including number of adherent cells, cell area, width-to-length ratio,
109 phosphorylated SLP76 (pSLP76) and F-actin intensity (Figure 1A). Natalizumab exposure led
110 to a reduction in cell spreading and in the intensities of the pSLP76 and F-actin stainings in
111 both CD4⁺ and CD8⁺ T-cell subsets (Figure 1B,C). The combination of the considered
112 descriptors through Principal Component Analysis (PCA) separated the natalizumab-treated
113 from the non-treated samples along component F1 (Figures 1B,C), indicating a robust effect of
114 natalizumab across the samples. The main descriptors that drove the segregation of treated
115 *versus* non-treated PBMCs along component F1 were pSLP76 intensity and width-to-length
116 ratio for CD4⁺ cells and cell area for CD8⁺ T cells (Table S1). Adhesion over VCAM-1 of both
117 CD4⁺ and CD8⁺ T-cell subsets was severely reduced upon natalizumab exposure in a consistent
118 way across the tested samples (Figures 1D, E). Natalizumab-induced reduction of cell area was
119 more frequent across the donors in CD8⁺ than CD4⁺ T cells. In contrast, the effects of
120 natalizumab on width-to-length ratio and F-actin intensity were more consistent across the
121 donors in CD4⁺ than CD8⁺ T cells, while pSLP76 intensity was decreased in both T-cell subsets.
122 Combined analysis of cell morphology, F-actin and pSLP76 intensities by automated confocal
123 microscopy is therefore an adapted approach to capture the sensitivity of T cells to *in vitro*
124 natalizumab exposure.

125

126

127 **CD8⁺ T cells from MS patients are highly sensitive to natalizumab exposure**

128 We next applied the HCI pipeline to PBMC samples from 40 persons with MS who had received
129 at least one first line of treatment but had not yet been treated with natalizumab at the time of
130 sample collection (BIONAT cohort ²⁹, see Table S2). In addition to CD4⁺ and CD8⁺ T-cell
131 subsets, we extended the evaluation of the *in vitro* effects of natalizumab on CD14⁺ monocytes
132 and CD19⁺ B cells due to the contribution of these leukocyte subsets to MS pathogenesis ³⁰.
133 Our analysis aimed at defining which subsets within MS PBMCs would be most affected by
134 natalizumab exposure (Figure 2A). A prominent effect of natalizumab exposure was the global
135 reduction of the spreading of MS PBMCs (Figure 2B), as observed with the HD T cells. When
136 considering the monocyte subset by gating on the CD14⁺ cells, our method was however not
137 able to clearly distinguish the natalizumab-exposed from the unexposed samples, as shown on
138 the PCA analysis (Figure 2C). A wide dispersion of the samples was observed when considering
139 CD19⁺ B cell and CD4⁺ T-cell subsets, with only a partial discrimination of the natalizumab-
140 exposed and unexposed samples (Figures 2D,E). Such discrimination occurred along the F1
141 component and was mainly driven by pSLP76 intensity (Table S3). The HCI pipeline separated
142 natalizumab-exposed and unexposed samples when considering the CD8⁺ T-cell subset, as
143 shown by the distribution along the F1 component of the PCA plot, also mainly driven by
144 pSLP76 intensity (Figure 2F and Table S3). Therefore, within the tested MS PBMC samples,
145 CD8⁺ T cells appeared to be the most sensitive cell subset to the effects of natalizumab exposure
146 as captured by our image-based approach. By analyzing the effect of natalizumab on the CD8⁺
147 T cells of the 40 patients, we observed a decrease in the number of adherent cells, in cell
148 spreading and in cell elongation, as well as a modest decrease in pSLP76 intensity (Figure 2G).
149 As previously observed with the HD PBMCs, F-actin intensity was not reduced in CD8⁺ T cells
150 from MS patients upon natalizumab exposure. These findings demonstrate the robustness of the
151 HCI method to capture sensitivity of MS patients' PBMCs to natalizumab. Furthermore, it
152 points to CD8⁺ T cells as the cellular subset exhibiting the most pronounced response to *in vitro*
153 natalizumab exposure.

154

155 **Unsupervised clustering of HCI data discriminates non-responder MS patients**

156 Based on the reasoning that *in vitro* natalizumab effects on T cells prior to treatment might
157 mirror the *in vivo* treatment efficacy, we next tested whether our HCI pipeline could detect
158 differences in pretreatment PBMC samples from patients that had responded favorably or not

159 to natalizumab treatment. For that purpose, we selected 40 patients from the BIONAT cohort,
160 corresponding to 20 responders and 20 non-responders to natalizumab therapy, based on the
161 NEDA-3 criteria (Table S2). Comparable levels of CD49d were expressed on the different
162 PBMC subsets from the 2 groups of patients, implying that VLA-4 expression does not by itself
163 determine the response to therapy (Figure S1). We applied our HCI pipeline to the pretreatment
164 PBMC samples, focusing on CD8⁺ T cells since they were identified in the optimization step
165 as the most responsive subset. We increased the sensitivity of the HCI pipeline by imaging the
166 samples with a 63X objective and harvesting an enriched set of 407 features based on intensity,
167 cell morphology (symmetry, threshold compactness, axial and radial distributions) and texture
168 elements (spots, edges, and ridges) of F-actin and pSLP76. We calculated, for each feature, the
169 difference in absolute value between the natalizumab-exposed and the natalizumab-unexposed
170 samples (mean across cells and wells), which was normalized (relative delta) to investigate the
171 effect of natalizumab on multiple features on the same scale (Figure S2). The unsupervised
172 PCA analysis segregated partially the non-responders' samples along the F1 component, with
173 18 of the 20 samples associated with negative F1 values (Figure 3B). T cells from a typical non-
174 responder patient displayed a reduced spreading upon natalizumab exposure while maintaining
175 a partially polarized shape (Figure 3B, top left image). T cells from the most divergent non-
176 responder patient exhibited increased cell width upon natalizumab exposure (Figure 3B, bottom
177 left image). Samples from responder patients occupied a rather dispersed distribution on the
178 PCA plot. Representative T cells from responder patients displayed a pronounced reduction of
179 cell spreading and an apparent loss of cell polarity upon natalizumab exposure (Figure 3B, top
180 right and bottom right). This analysis suggests that CD8⁺ T cells from the non-responder
181 patients were less sensible to *in vitro* natalizumab exposure in terms of cell morphology
182 alterations. The discrimination of non-responder samples was further confirmed by a
183 complementary unsupervised K-means clustering analysis built from the 407 features that
184 identified 2 clusters, including one that gathered 18 of the 20 samples from the non-responder
185 patients (Figure 3C). In agreement with the PCA analysis, the samples from the responder
186 patients distributed among the two clusters. Parallel PCA and K-means analysis on the CD4⁺
187 T-cell compartment failed to indicate segregation (Figures S4A, B). We further applied a Ward
188 clustering approach, built from the 50 most important features from the PCA (Table S4), which
189 segregated the samples in two main branches, with one gathering 15 of the 20 samples from the
190 non-responder patients (Figure 3D). This branch was characterized by a majority of features,
191 which values were poorly impacted by natalizumab exposure, as opposed to the branch
192 composed of a majority of responder samples. These features included Axial small length, Cell

193 and Nucleus area, Cell width and multiple F-actin and p-SLP76 texture related descriptors
194 (Figure 3D, Table S4). On the other hand, a minority of discriminative features had values that
195 were highly reduced by natalizumab exposure in the non-responder branch, as Actin symmetry
196 03 SER-spot, that can be interpreted as actin dots uniformly distributed in three parts of the
197 considered cells. Analysis of Actin axial small length (Figure 3E), which was reduced by
198 natalizumab in cells from responders, and Actin profile 1/5 SER-saddles (Figure 3F), which
199 was impacted by natalizumab in cells from non-responders, illustrates how the cells from the
200 two patient groups may distinctly remodel their F-actin cytoskeleton upon natalizumab
201 exposure. Together, this unsupervised morphological analysis indicates that CD8⁺ T cells from
202 non-responder patients tend to display reduced loss of cell spreading and polarity upon *in vitro*
203 exposure to natalizumab.

204

205 **Prediction of natalizumab treatment outcome with a machine learning model**

206 As the unsupervised analysis indicated a partial discrimination of responder and non-responder
207 patients based on how natalizumab impacted CD8⁺ T-cell features, we implemented a machine
208 learning approach to investigate whether samples from responder and non-responder patients
209 could be distinguished. We opted for a Random Forest (RF)-based approach that trained
210 individual models with the features from the image dataset generated from the 40 MS patient
211 samples, labeled as discovery cohort (Figure 4A). Redundant features displaying >90%
212 correlation were first removed, reducing the number of features to 133. Based on 1024 different
213 combinations used to train the estimators, the RF-based approach generated 33 combinations
214 of features that could distinguish responders from non-responders with F1-score and accuracy
215 higher than 90% (Figure 4B). Surpassing the threshold of 70% performance in each of these
216 scores is indicative of an efficient discrimination. Among the ten most important features, five
217 were related to actin segmentation, symmetry and texture, one to pSLP76 distribution symmetry
218 and texture and one to cell morphology (Figures 4C, S4, S5). In addition to the importance, we
219 also analyzed how often each feature appeared in decision tree combinations that lead to a F1
220 score higher than 90%. Except for Actin profile 5/5 SER-hole and pSLP76 symmetry 05 SER-
221 dark, all features had frequencies above 50% (Figure 4C), suggesting that their combined
222 integration was key for discriminating samples. To challenge the robustness of the HCI
223 approach to predict treatment response, it was applied to a validation group of 28 patients,
224 denominated validation cohort, composed of 14 responders and 14 non-responders (Table S5).

225 We tested the same 1024 combinations of features to evaluate their performance on the
226 validation cohort using the 10 most important features as identified through the analysis of the
227 discovery cohort. The most accurate combinations were associated with a F1 score of 77% and
228 an accuracy of 66% (Figure 4D). The two features with low frequencies in combinations in the
229 discovery cohort (Actin profile 5/5 SER-hole and pSLP76 symmetry 05 SER-dark) also
230 displayed low frequencies in the validation cohort (Figure 4E). To further investigate how those
231 ten features were discriminating the two groups of patients, we combined the two cohorts and
232 evaluated, for each feature, the p value pertaining to the comparison of the effect of natalizumab
233 on cells from responders and non-responders (Figure 4F). Actin profile 2/5 SER-saddle and
234 Nucleus area were the two features with $p < 0.05$ that also had consistent importance and
235 frequency among the two cohorts, suggesting that those two features were the most
236 discriminative ones. The impact of natalizumab on the reduction of nucleus area was barely
237 detected in most of the non-responder patients (Figure 4G). This may reflect the propensity of
238 natalizumab to impair T-cell spreading on VCAM-1. On the other hand, natalizumab exposure
239 resulted in a decrease of the Actin profile 2/5 SER-saddle feature in most of the non-responder
240 samples but not in the responder samples (Figure 4H). This is suggestive of a specific
241 remodeling of the actin cytoskeleton (smoother distribution of F-actin in the cellular
242 compartment corresponding to the cytoplasm, see Figure S5), upon natalizumab exposure in
243 the CD8⁺ T cells from the non-responders. The combination of our HCI-based analysis with a
244 supervised model therefore provides a proof-of-concept that patient-specific responses to
245 natalizumab can be captured *in vitro* prior to treatment in a way to predict the *in vivo* treatment
246 response.

247

248 **CD8⁺ T cells from non-responder patients tend to resist the impact of VLA-4 blockade on** 249 **cell spreading**

250 To gain insight into the biological underpinnings of the diverging therapeutic responses, we
251 sought to further explore the meaning of the individual discriminative features. We combined
252 the data from the two cohorts, ranked features according to the p value of the responder/non-
253 responder comparison and completed our analysis of T-cell response to natalizumab by live cell
254 imaging (Figure 5A). Among the 407 features, 29 presented a $p \text{ value} < 0.05$ (Table S6). For
255 each feature, we calculated and normalized the effect of natalizumab for the responder and non-
256 responder subgroups (relative Δ) and then computed the difference of relative Δ between the 2

257 subgroups (Figure 5B, X axis). This analysis clearly segregated features into those associated
258 with a more pronounced effect of natalizumab on T cells from responder patients (Figure 5B,
259 right side of the chart) and those associated with a more pronounced effect of natalizumab on
260 T cells from non-responder patients (Figure 5B, left side of the chart). Morphology features
261 (cell and nucleus area, cell width) were exclusively found in the first set of features, confirming
262 the notion that T cells from non-responder patients are more resistant to natalizumab-induced
263 reduction of cell spreading and elongation (see Figure 5C-D for individual patient values for
264 cell area and cell width). On the other hand, features related to actin texture and distribution
265 were almost exclusively found in the second set of features. This highlights that CD8⁺ T cells
266 from non-responder patients tend to be less susceptible to natalizumab by resisting the impact
267 of VLA-4 blockade on cell spreading and polarity, but also by adopting a specific actin
268 cytoskeleton organization. The nature of the actin-related features (e.g. actin ridges and valleys)
269 implies that natalizumab evoked a more homogenous distribution of F-actin in T cells from
270 non-responder patients, both at the cell periphery and towards the center of the adhesion plane
271 (Figure 5E,F). The biased organization of F-actin in T cells from non-responders was not
272 associated to a difference in F-actin levels (Figure S6). We next asked how the morphological
273 and actin remodeling effects of natalizumab on T cells from responder and non-responder
274 patients may translate into their ability to migrate over VCAM-1. For that purpose, we evaluated
275 morphology, velocity, and straightness of CD8⁺ T cells from four patients from each treatment
276 response subgroup, upon interaction with VCAM-1 in an under-agarose setting to prevent non-
277 specific cell displacements. T cells tended to form homotopic aggregates upon natalizumab
278 exposure (Figure 5G), as previously reported for other anti-VLA-4 antibodies^{19,30}, but this
279 phenomenon appeared to impact comparably T cells from both subgroups (Figure 5H). Analysis
280 of cell area confirmed that T cells from non-responders tend to be resistant to the reduction of
281 cell spreading evoked by natalizumab (Figure 5I). Interestingly, tracking analysis indicated that
282 intrinsic velocity and ability to migrate along straight paths, rather than response to natalizumab
283 *per se*, were the parameters that distinguished T cells from the considered responders and non-
284 responders (Figures 5J, K). This complementary live microscopy assay therefore suggests that
285 intrinsic differences in the propensity to migrate over VCAM-1 might differentially predispose
286 T cells to the activity of natalizumab. Collectively, our analysis points to a multi-parametric
287 origin of the variable sensitivity of MS patient CD8⁺ T cells to natalizumab, including intrinsic
288 determinants related to cell motility, resistance to natalizumab in terms of cell spreading
289 inhibition and actin remodeling upon natalizumab exposure.

290 Discussion

291 Although natalizumab has revolutionized the treatment of relapsing-remitting MS, a substantial
292 proportion of treated patients experience disease relapse. The incomplete response rate (30%)
293 to natalizumab treatment at one year, and even more thereafter ¹⁷, carries a high societal and
294 human burden to health institutions and to the patients and their families. In this context,
295 strategies to predict natalizumab efficacy would allow for the implementation of personalized
296 treatment schemes. Multiple parameters have been proposed to account for treatment failure in
297 individual patients. Given the multiplicity of cellular subsets expressing $\alpha 4$ integrin subunit and
298 the multiplicity of cellular activities that VLA-4 blockade through natalizumab may alter,
299 identifying a biomarker to discriminate and eventually predict individual patient response has
300 remained challenging. Herein, we designed a high-content image-based approach applied to
301 human PBMCs to monitor, through multiple morphological and molecular parameters, the
302 sensitivity of patient cells to natalizumab upon *ex vivo* exposure. We further tested whether
303 such *ex vivo* challenge would capture inter-individual variability that might align with the
304 clinical outcomes of individual MS patients treated with natalizumab.

305 In the context of personalized medicine, HCI is emerging as a unique approach that captures
306 simultaneously molecular information and cellular morphometrics with single cell resolution.
307 The application of HCI in drug testing workflows might generate results within a few days ³¹
308 and deliver treatment efficacy prediction with high prediction accuracy ³². The potential of HCI
309 to provide support for treatment decision has recently been highlighted by its ability to predict
310 drug efficacy in patients with hematological cancers ^{33,34}. Here, we took the challenge of testing
311 whether HCI might be applicable to screen the efficacy of a therapeutic antibody on non-
312 neoplastic immune cells in the context of an auto-immune disease. Differently from previous
313 HCI studies that monitored tumor cell viability and global activity of surrounding immune cells,
314 our approach was tailored to assess the specific activity of the VLA-4-targeting antibody
315 natalizumab, by stimulating PBMC from persons with MS on VCAM-1 and exposing them to
316 natalizumab. We opted for high-resolution confocal acquisition, aiming to precisely capture
317 individual cell morphological features, as well as parameters related to F-actin organization and
318 SLP76 distribution, given the central position of these molecular activities in the response of
319 leukocytes to VLA-4 engagement. Instead of extracting predefined sets of parameters, we
320 applied clustering and machine learning methods to hundreds of parameters to take full
321 advantage of the rich image datasets.

322 We provide evidence that such approach focused on the mechanism of action of natalizumab
323 presents with several advantages compared to what has been achieved so far in terms of
324 natalizumab response prediction: timing of prediction, cohort size, statistic strength and
325 biological explanation. Several studies have aimed at predicting the efficacy of natalizumab
326 treatment. High anti-phosphatidylcholine IgM levels in the serum were associated to treatment
327 response in a study involving 33 patients ¹⁹. Decreased levels of B cells and intrathecal
328 immunoglobulin synthesis in the cerebrospinal fluid were also associated with optimal response
329 through the evaluation of 23 patients under treatment ²¹. Another study involving 30 patients
330 under natalizumab treatment pointed to a decrease of metalloproteinases serum levels in
331 patients with no relapse episodes ²⁰. Two studies performed with 29 and 49 patients under
332 treatment pointed to CD49d expression in leukocytes as a biomarker for determining optimal
333 dose and predicting treatment efficacy ^{35 18}. Our analysis conducted on PBMC samples prior
334 to treatment however failed to establish a link between CD49d expression and natalizumab
335 treatment efficacy, potentially reflecting that the profile of CD49d expression might be altered
336 during the treatment. Finally, age and disease duration at treatment initiation were identified as
337 parameters affecting treatment response in a study of 48 patients ²². These studies were
338 conducted with classical statistical analysis by evaluating the fitness of individual biological or
339 patient-related parameters. They suffered from not evaluating the robustness of the considered
340 parameters in independent cohorts. Most of them were conducted in the course of treatment and
341 did not evaluate the predictive value of the considered parameters before treatment initiation.
342 In this context, our approach proposes a paradigmatic shift in the search for a treatment efficacy
343 predictor. By combining a miniaturized and automatized image-based bioassay and machine
344 learning approaches, we extract individual patient signatures directly reflecting the quantitative
345 and qualitative impact of natalizumab on primary cells from the patients. It reached a prediction
346 power above 70% and presents predictive values of accuracy and F1-score comparable or above
347 those of other studies that applied machine learning methods to predict clinical outcome in other
348 disease settings ^{36,37}. We anticipate that our workflow could be generalized to the testing of
349 other therapeutic antibodies across multiple clinical indications.

350 The HCI pipeline identified CD8⁺ T cells as the most prominent subpopulation to predict
351 response to natalizumab. The CD8⁺ T-cell subset was previously suggested as a cell population
352 to predict PML development risk from MS patients ³⁸. We failed to detect substantial effects of
353 natalizumab exposure on monocytes. This finding might agree with the natalizumab-induced
354 upregulation of $\alpha 4$ on monocytes ³⁹ contrasting with the downregulation of $\alpha 4$ on lymphocytes

355 ¹⁸. Despite the VLA-4 mediated role of B cells in MS neuroinflammation ⁴⁰, our study did not
356 point B cells as a critical population to determine natalizumab effect and predict patient
357 response. The prediction of natalizumab patient clinical outcome by machine learning was
358 mainly driven by a set of actin related features associated to how CD8⁺ T cells adhere, enrich,
359 and distribute actin at the adhesion plane, spread and elongate on VCAM-1. The role of
360 integrins in promoting cell spreading and their implication in many diseases are well established
361 ⁴¹⁻⁴³. The HCI pipeline leads to the identification that non-responder patients are resistant to
362 natalizumab-induced decrease on cell spreading and elongation, which are morphological
363 adaptations needed to allow T-cell interstitial migration through the adaptation and formation
364 of motility related structures such as the lamellipodia and the uropod ⁴⁴. Our data point to an
365 increased migratory profile of the CD8⁺ T cells from the non-responder patients. Thus, we
366 hypothesize that by preserving cell spreading ability, non-responder CD8⁺ T cells have an
367 increased capacity to transmigrate towards the CNS and to establish IS with target cells leading
368 to cell killing and consequent inflammation in the CNS.

369 Our study showcases how HCI combined to machine learning algorithms may serve as a
370 treatment testing platform to guide treatment prescription. The less sophisticated measurement
371 of a single key biological marker might sound as a most desirable approach. However, our study
372 clearly indicates that among many considered parameters, none could by itself be discriminative
373 enough to predict treatment outcome. Since automated high-content cell imagers are becoming
374 increasingly available in the technological portfolio of biomedical research centers, the
375 development of standardized bioassays based on this technology might become feasible in a
376 near future.

377

378 **Limitations of the study**

379 Despite the potential of our analysis in coupling HCI of patient PBMCs to machine learning
380 algorithms and providing biological interpretation, validation in larger cohorts across multiple
381 clinical centers would be necessary before translation in medical practice. In this study we have
382 not investigated whether a more precise examination of the effects of natalizumab on various
383 T-cell subsets might have revealed selective effects and increased the prediction power of our
384 approach. We have also not tested whether our pipeline might predict the risk of developing
385 serious side-effects such as PML. Finally, to reinforce the relevance of the HCI approach, it
386 will be interesting to study how the distinct morphological and actin remodeling effects of

387 natalizumab on T cells from responder and non-responder patients may be sustained by distinct
 388 molecular responses and translate into distinct motility capacities.

389

390 **Methods**

391 **Materials**

Reagent or resource	Source	Identifier
Antibodies		
Natalizumab	Biogen	Tysabri
Recombinant Anti-SLP76 (phospho Y145) antibody [EP2853Y]	Abcam	ab75829
Zombie NIR™ Fixable Viability Kit	Biolegend	423105
Human CD4 Antibody	R&D Systems	MAB3791
Human CD8 alpha Antibody	R&D Systems	MAB3803
CD14 antibody [TÜK4	Biorad	MCA1568T
Human CD19 Antibody	R&D Systems	MAB4867
Goat anti-Rabbit IgG (H+L) Highly Cross-Adsorbed Secondary Antibody, Alexa Fluor™ 647	ThermoFisher	A21245
Goat anti-Mouse IgG1 Cross-Adsorbed Secondary Antibody, Alexa Fluor™ 546	ThermoFisher	A21123
Goat anti-Mouse IgG2a Cross-Adsorbed Secondary Antibody, Alexa Fluor™ 546	ThermoFisher	A21133
Recombinant and purified proteins		
Recombinant human IL-2	Peptotech	200-02
Recombinant Human VCAM-1/CD106 Protein	R&D Systems	ADP5
Medium components, buffers, and chemicals		
RPMI 1640 Medium with GlutaMAX	Gibco	21875-034
Human serum (AB)	Institut de Biotechnologies Jacques Boy	201021334
Penicillin/streptomycin	Gibco	15140-122
Sodium pyruvate	Gibco	11360070
MEM Non-Essential Amino Acids Solution	Gibco	11140050
HEPES	Gibco	15630-056
Phytohemagglutinin (PHA-P)	ThermoFisher Scientific	R30852801
Permeabilization Buffer (PB)	eBioscience	00-8333-56
Paraformaldehyde (PF)	ThermoFisher Scientific	50-980-489
Alexa Fluor™ 546 Phalloidin	ThermoFisher	A21123
Alexa Fluor™ 488 Phalloidin	ThermoFisher	A12379
DAPI (4',6-Diamidino-2-Phenylindole, Dihydrochloride)	ThermoFisher	D1306
CellTrace™ Calcein Red-Orange, AM	ThermoFisher	C34851
CellTracker™ Green CMFDA Dye	ThermoFisher	C2925

CD8 ⁺ T Cell Isolation Kit, human	Miltenyi Biotec	130-096-495
Plates		
384-well plate CellCarrier-384 Ultra	Perkin Elmer	6057302
Equipment		
High-content screening system (Opera Phenix)	Perkin Elmer	N/A
BD LSR Fortessa Cytometer	BD Biosciences	N/A
MACsQuant VYB cytometer	Miltenyi Biotec	N/A
Softwares		
Fiji ImageJ software	NIH	N/A
TrackMate tool in ImageJ	N/A	N/A
Harmony software	Perkin Elmer	N/A
GraphPad Prism v8.0.2	N/A	N/A
XLSTAT Basic 2022.5.1	N/A	N/A
Scikit 1.2.2	N/A	N/A
FlowJo 10.8.1	N/A	N/A

392

393 **Experimental model and subjects' details**

394 PBMCs from healthy donors (HD): frozen PBMCs from 10 HD were obtained from The
395 Etablissement Français du Sang. The corresponding blood samples were collected following
396 standard ethical procedures (Helsinki protocol) and as per French Bioethics law. The work on
397 PBMCs conducted in this study was covered by an approval by the local ethics committee
398 (Comité de Protection des Personnes Sud-Ouest II et Outre-Mer II). PBMCs were thawed in
399 RPMI-based growth media (RPMI media (Gibco), 5% human serum (heat inactivated, AB
400 positive blood type, Institut de Biotechnologies Jacques Boy), 100 U/ml penicillin/streptomycin
401 (Gibco), 1 mM sodium pyruvate (Gibco), 1X MEM non-essential amino acids (Sigma), 10 mM
402 HEPES (Gibco). Cell culture was maintained at 37°C and 5% CO₂. Cellular composition was
403 analyzed by measuring CD3, CD49d, CD4 and CD8 expression by flow cytometry.

404 PBMCs from persons with MS: frozen PBMCs from 68 MS patients were obtained from the
405 BIONAT cohort [26]. Patient samples were collected in accordance with law n° 2004-806 of
406 August 9, 2004 relating to public health policy. This research received a favorable opinion from
407 the Committee for the Protection of Persons (CPP) Sud Ouest et Outre Mer II on 06/02/2009,
408 received authorization from the competent authority on 09/02/2009, and was declared to the
409 Commission Nationale Informatique et Libertés (CNIL). The registration number at
410 ClinicalTrials.gov is NCT00942214. The herein studied blood samples were collected prior to
411 natalizumab treatment, from which PBMCs were prepared and frozen. Samples were thawed in
412 RPMI media 5% human serum maintained for 16 h at 37 °C and 5% CO₂ before being processed
413 through the HCI workflow. Details for each patient are available in Tables S2 and S4. Cellular
414 composition was analyzed by measuring CD3, CD49d, CD4 and CD8 expression by flow
415 cytometry.

416 NEDA-3 classification: classification into responder or non-responder patients was performed
417 according to the NEDA-3 score ⁴⁵. No Evidence of Disease Activity-3 is calculated based on
418 the absence of clinical relapses, confirmed disability progression, and new or enlarging lesions
419 on brain magnetic resonance imaging. If a person with MS under treatment has experienced no
420 clinical relapse, no confirmed disability worsening and no new lesions during 2 years, he/she is
421 considered as responder to natalizumab therapy.

422 CD8⁺ T cells from MS patients: From the obtained PBMC, cells were kept in culture for 5 days
423 in the presence of IL-2 and PHA. CD8⁺ T cells were then purified using CD8⁺ T Cell Isolation
424 Kit.

425

426 **High-content cell imaging of PBMCs from HD**

427 **Staining:** A high-content screening 384-well imaging plate (CellCarrier-384 Ultra, Perkin
428 Elmer) was coated overnight at 4°C with VCAM-1 (R&D Systems) at 0.625 µg/mL. The plate
429 was then washed with phosphate-buffered saline (PBS) and cell culture medium. Freshly
430 thawed PBMCs from 10 HD were centrifuged at 430 g for 5 min, split in two and natalizumab
431 (Biogen) was added in part of the cells at the final concentration of 2 µg/mL. Cells were
432 incubated for 30 min at 37°C and 5% CO₂. Next, cells were washed to remove antibody excess.
433 A total of 9000 cells/30 µL were seeded per well of the 384-well precoated plate, followed by
434 a 10 s centrifugation. After stimulation for 10 min at 37°C, non-adherent cells were removed
435 by flipping the plate. Subsequently, the cells were fixed using 3% paraformaldehyde (PFA),
436 washed with PBS and permeabilization buffer (PB, eBioscience), and then stained with Alexa
437 Fluor™ 488 Phalloidin (ThermoFisher), anti-pSLP76 antibody and anti-CD4 or anti-CD8
438 antibodies (R&D systems) The plate was incubated overnight at 4°C. The plate was then
439 washed with PB and stained with anti-Rabbit Alexa647 (ThermoFisher), anti-mouse IgG2a
440 Alexa 546 antibodies and 4',6-Diamidino-2-Phenylindole, Dihydrochloride (DAPI,
441 ThermoFisher). After 1 h incubation, the plate was washed three times with PBS and subjected
442 to automated confocal imaging.

443 **Acquisition:** Images were acquired with a high-content screening system (Opera Phenix,
444 PerkinElmer) equipped with a 40x 1.1 NA Plan Aplanachromat water immersion objective, 4
445 sCMOS cameras (2160x2160 pixels, 16 bits, 6.5 µm pixel) and a Yokogawa spinning disk
446 confocal unit. For each well, 49 fields-of-view and 4 Z-planes per field (with step of 0.5 µm,
447 starting at the cell contact plane with the substrate) were acquired. Z-stacks of images were
448 projected along Z-axis using maximum intensity global projection and flatfield correction using
449 Harmony software. Z-projected data were then processed with the same software. First, nuclei
450 were located via DAPI staining using thresholding on the staining intensity. The cell cytoplasm
451 were identified by thresholding on the 488 Phalloidin staining. CD4⁺ and CD8⁺ T cells were
452 identified by thresholding on the CD4 and CD8 stainings. Number of detected cells, cell area,
453 cell width to length, pSLP76 and F-actin mean intensities were extracted separately for the
454 CD4⁺ and CD8⁺ T-cell subsets with Harmony software.

455

456 **High-content cell imaging of PBMCs from MS patients**

457 **Staining:** The HCI workflow described above for HD samples was adapted for MS samples
458 with the following modifications. Imaging plates were coated with 1.25 µg/mL VCAM-1. A
459 total of 27000 cells were seeded in each well and stimulated for 10 min at 37°C, before fixation.
460 Cells were stained overnight at 4°C with α-pSLP76 antibody (Rabbit ab75829), Phalloidin 488
461 (A12379) and either α-CD4 antibody (IgG2a MAB3791), or α-CD8 antibody (IgG2a
462 MAB3803), or α-CD14 antibody (IgG2a MCA1568T), or α-CD19 antibody (IgG1 MAB4867).
463 The secondary staining step consisted in α-rabbit Alexa 647 (A21245), DAPI and either α-IgG1
464 Alexa 546 (A21123) or α-IgG2a Alexa 546 (A21133).

465 **Acquisition:** Plates were subjected to 2 rounds of confocal imaging with a 20x 0.4 NA Plan
466 Aplanachromat air objective (25 fields-of view covering the entire well) and a 63x 1.15 NA Plan
467 Aplanachromat water immersion objective (56 fields-of view). The subpopulations of PBMCs
468 were segregated by thresholding for the staining intensity of the relevant staining (CD4 for
469 CD4⁺ T cells, CD8 for CD8⁺ T cells, CD14 for monocytes and CD19 for B cells).
470 Morphological filters (cell and nucleus area) were added to further distinguish lymphocytes
471 from monocytes. Once the populations were defined, basic morphological and intensity
472 parameters were extracted with Harmony software. For the images acquired with the 63x
473 objective, the analysis was enriched by applying the SER and STAR methods of Harmony on
474 the F-actin and pSLP76 stainings. This resulted in library of 407 features per cell.

475

476 **Under agarose migration of CD8⁺ T cells from MS patients**

477 A 384-well plate was coated with VCAM-1 (0.625 µg/mL) at 4°C overnight, then rinsed with
478 PBS before cell culture medium was added to accommodate the cells. To produce a confined
479 environment, a 50 µL layer of 0.5% agarose in RPMI was placed in each well used for the
480 assay. CD8⁺ T cells from 4 responders patients and 4 non-responders patients were collected,
481 centrifuged (10 min 122g) and resuspended in RPMI. Responders' cells were stained with
482 Calcein Red-Orange and non-responders' cells were stained with CellTracker™ Green
483 CMFDA. After incubation at 37°C for 30 minutes and centrifugation, cells were resuspended
484 in RPMI medium containing 5% human serum. Pairs of non-responder/responder cells were
485 formed and mixed gently and adjusted for a concentration of 25,000 cells from each patient per
486 10 µL. Natalizumab was added in a final concentration of 2 µg/mL and cells were then injected
487 under the agarose layer. The plate was then incubated for 30 minutes at 37°C with 5% CO₂, and
488 the microscope's (Opera Phenix, PerkinElmer) temperature and CO₂ levels were adjusted
489 accordingly. An 8-hour acquisition phase followed, capturing images of the entire well at 1-
490 minute intervals at 10x magnification. The resulting images from the first 2 h were then
491 processed using the cell tracking tool from Harmony software, and validated by TrackMate tool
492 in ImageJ, to extract relevant cell motility parameters, allowing for the accurate quantification
493 of cell migration.

494

495 **Statistical information**

496 **Unsupervised analysis for sample discrimination based on natalizumab therapy response**

497 The unsupervised analyses were performed using XLSTAT Basic 2022.5.1. The PCA was done
498 using correlation (Pearson) type, with a maximum of 5 calculated components. The chosen
499 component was based on the highest % to explain system variability. The K-mean clustering
500 was calculated using Euclidian distance dissimilarity index, Determinant (W) clustering
501 criterion with a maximum of 10 clusters. The number of clusters selected to explain the results
502 was based on the highest Silhouette score. To validate the number of clusters pointed by the
503 silhouette scores, hierarchical ascendent classification was also performed. The clustering was
504 considered only if both analyses lead to the same result.

505

506 **Machine Learning-based analysis for feature combination in natalizumab therapy** 507 **response**

508 A Random Forest Classifier (RFC) was embedded in the Scikit-learn python library v1.2.0⁴⁶.
509 We independently analyzed the 407 features from both the discovery and validation cohorts.
510 The datasets were split into 70:30 training and test samples for the first (n=28:12) and second
511 (n=19:9) cohorts, while ensuring a stratified distribution of the classes. For each unique
512 combination of features, we trained a separate RFC model. The RFC hyperparameters for each
513 model were tuned using the GridSearchCV function with 10-fold cross-validation. The
514 evaluation focused on combinations with the highest F1-Score. To remove redundancies, we
515 removed features having >90% correlation, leading us to retain 133 features in the first cohort.
516 We subseted the second cohort with the most important features selected on the first cohort to
517 train individual models for each combination, subsequently evaluating their performance
518 metrics.

519

520 **Statistical analysis and graphical representations**

521 For all experiments, except for the supervised and unsupervised analysis and the bubble chart,
522 the resulting data were subjected to quantification and statistical analysis using GraphPad Prism
523 v8.0.2. The heatmap (Figure 3D) was generated by SRPLOT server and the bubble chart (Figure
524 5B) was generated by Visual Paradigm server. Specific details regarding the statistical tests
525 employed, representation of significance, and number of experimental data points are provided
526 in the corresponding figure legends.

527

528 **Data availability**

529 Additional information and requests for resources should be directed to and will be fulfilled by
530 the lead contact, Loïc Dupré (loic.dupre@inserm.fr)

531

532 **References**

- 533 1. Hemler, M. E., Elices, M. J., Parker, C. & Takada, Y. Structure of the integrin VLA-4
534 and its cell-cell and cell-matrix adhesion functions. *Immunol Rev* **114**, 45–65 (1990).
- 535 2. Alon, R. *et al.* The integrin VLA-4 supports tethering and rolling in flow on VCAM-1.
536 *Journal of Cell Biology* **128**, 1243–1253 (1995).
- 537 3. Mittelbrunn, M. *et al.* VLA-4 integrin concentrates at the peripheral supramolecular
538 activation complex of the immune synapse and drives T helper 1 responses. *Proceedings*
539 *of the National Academy of Sciences* **101**, 11058–11063 (2004).
- 540 4. Nguyen, K., Sylvain, N. R. & Bunnell, S. C. T Cell Costimulation via the Integrin VLA-
541 4 Inhibits the Actin-Dependent Centralization of Signaling Microclusters Containing the
542 Adaptor SLP-76. *Immunity* **28**, 810–821 (2008).

- 543 5. Kim, T. K., Billard, M. J., Wieder, E. D., McIntyre, B. W. & Komanduri, K. V.
544 Coengagement of $\alpha 4\beta 1$ integrin (VLA-4) and CD4 or CD8 is necessary to induce
545 maximal Erk1/2 phosphorylation and cytokine production in human T cells. *Hum*
546 *Immunol* **71**, 23 (2010).
- 547 6. Pyka-Fościak, G., Lis, G. J. & Litwin, J. A. Adhesion Molecule Profile and the Effect of
548 Anti-VLA-4 mAb Treatment in Experimental Autoimmune Encephalomyelitis, a Mouse
549 Model of Multiple Sclerosis. *Int J Mol Sci* **23**, 4637 (2022).
- 550 7. Elovaara, I. *et al.* Adhesion Molecules in Multiple Sclerosis: Relation to Subtypes of
551 Disease and Methylprednisolone Therapy. *Arch Neurol* **57**, 546–551 (2000).
- 552 8. Schläger, C. *et al.* Effector T-cell trafficking between the leptomeninges and the
553 cerebrospinal fluid. *Nature* **530**, 349–353 (2016).
- 554 9. Schneider-Hohendorf, T. *et al.* VLA-4 blockade promotes differential routes into human
555 CNS involving PSGL-1 rolling of T cells and MCAM-adhesion of TH17 cells. *J Exp*
556 *Med* **211**, 1833 (2014).
- 557 10. Charabati, M. *et al.* DICAM promotes TH17 lymphocyte trafficking across the blood-
558 brain barrier during autoimmune neuroinflammation. *Sci Transl Med* **14**, (2022).
- 559 11. Yednock, T. A. *et al.* Prevention of experimental autoimmune encephalomyelitis by
560 antibodies against $\alpha 4\beta 1$ integrin. *Nature* **356**, 63–66 (1992).
- 561 12. Yang, G. X. & Hagmann, W. K. VLA-4 antagonists: potent inhibitors of lymphocyte
562 migration. *Med Res Rev* **23**, 369–392 (2003).
- 563 13. Schwab, N. & Wiendl, H. Learning CNS immunopathology from therapeutic
564 interventions. *Sci Transl Med* **15**, (2023).
- 565 14. Polman, C. H. *et al.* A Randomized, Placebo-Controlled Trial of Natalizumab for
566 Relapsing Multiple Sclerosis. *New England Journal of Medicine* **354**, 899–910 (2006).
- 567 15. Martin-Blondel, G. *et al.* Migration of encephalitogenic CD8 T cells into the central
568 nervous system is dependent on the $\alpha 4\beta 1$ -integrin. *Eur J Immunol* **45**, 3302–3312 (2015).
- 569 16. Havrdova, E. *et al.* Effect of natalizumab on clinical and radiological disease activity in
570 multiple sclerosis: a retrospective analysis of the Natalizumab Safety and Efficacy in
571 Relapsing-Remitting Multiple Sclerosis (AFFIRM) study. *Lancet Neurol* **8**, 254–260
572 (2009).
- 573 17. Prosperini, L., Fanelli, F. & Pozzilli, C. Long-term assessment of No Evidence of
574 Disease Activity with natalizumab in relapsing multiple sclerosis. *J Neurol Sci* **364**, 145–
575 147 (2016).
- 576 18. Defer, G. *et al.* CD49d expression as a promising biomarker to monitor natalizumab
577 efficacy. *J Neurol Sci* **314**, 138–142 (2012).
- 578 19. Muñoz, Ú. *et al.* Serum levels of IgM to phosphatidylcholine predict the response of
579 multiple sclerosis patients to natalizumab or IFN- β . *Sci Rep* **12**, (2022).

- 580 20. Balasa, R. *et al.* The Matrix Metalloproteinases Panel in Multiple Sclerosis Patients
581 Treated with Natalizumab: A Possible Answer to Natalizumab Non- Responders. *CNS*
582 *Neurol Disord Drug Targets* **17**, 464–472 (2018).
- 583 21. Villar, L. M. *et al.* Immunological markers of optimal response to natalizumab in
584 multiple sclerosis. *Arch Neurol* **69**, 191–197 (2012).
- 585 22. Sargento-Freitas, J., Batista, S., MacArio, C., Matias, F. & Sousa, L. Clinical predictors
586 of an optimal response to natalizumab in multiple sclerosis. *Journal of Clinical*
587 *Neuroscience* **20**, 659–662 (2013).
- 588 23. Bloomgren, G. *et al.* Risk of natalizumab-associated progressive multifocal
589 leukoencephalopathy. *N Engl J Med* **366**, 1870–1880 (2012).
- 590 24. German, Y. *et al.* Morphological profiling of human T and NK lymphocytes by high-
591 content cell imaging. *Cell Rep* **36**, (2021).
- 592 25. Severin, Y. *et al.* Multiplexed high-throughput immune cell imaging reveals molecular
593 health-associated phenotypes. *Sci Adv* **8**, 5631 (2022).
- 594 26. Kropivsek, K. *et al.* Ex vivo drug response heterogeneity reveals personalized
595 therapeutic strategies for patients with multiple myeloma. *Nature Cancer* **2023** *4:5* **4**,
596 734–753 (2023).
- 597 27. Vicente-Manzanares, M. & Sánchez-Madrid, F. Role of the cytoskeleton during
598 leukocyte responses. *Nature Reviews Immunology* vol. 4 110–122 Preprint at
599 <https://doi.org/10.1038/nri1268> (2004).
- 600 28. Hyduk, S. J. & Cybulsky, M. I. $\alpha 4$ Integrin Signaling Activates Phosphatidylinositol 3-
601 Kinase and Stimulates T Cell Adhesion to Intercellular Adhesion Molecule-1 to a Similar
602 Extent As CD3, but Induces a Distinct Rearrangement of the Actin Cytoskeleton. *The*
603 *Journal of Immunology* **168**, 696–704 (2002).
- 604 29. Outteryck, O. *et al.* A prospective observational post-marketing study of natalizumab-
605 treated multiple sclerosis patients: clinical, radiological and biological features and
606 adverse events. The BIONAT cohort. *Eur J Neurol* **21**, 40–48 (2014).
- 607 30. Pulido, R. *et al.* Functional evidence for three distinct and independently inhibitable
608 adhesion activities mediated by the human integrin VLA-4. Correlation with distinct
609 alpha 4 epitopes. *J Biol Chem* **266**, 10241–5 (1991).
- 610 31. Malani, D. *et al.* Implementing a Functional Precision Medicine Tumor Board for Acute
611 Myeloid Leukemia. *Cancer Discov* **12**, 388–401 (2022).
- 612 32. Snijder, B. *et al.* Image-based ex-vivo drug screening for patients with aggressive
613 haematological malignancies: interim results from a single-arm, open-label, pilot study.
614 *Lancet Haematol* **4**, e595–e606 (2017).
- 615 33. Kornauth, C. *et al.* Functional Precision Medicine Provides Clinical Benefit in Advanced
616 Aggressive Hematologic Cancers and Identifies Exceptional Responders. *Cancer Discov*
617 **12**, 372–387 (2022).

- 618 34. Kropivsek, K. *et al.* Ex vivo drug response heterogeneity reveals personalized
619 therapeutic strategies for patients with multiple myeloma. *Nature Cancer* 2023 4:5 4,
620 734–753 (2023).
- 621 35. Granell-Geli, J. *et al.* Assessing Blood-Based Biomarkers to Define a Therapeutic
622 Window for Natalizumab. *Journal of Personalized Medicine* 2021, Vol. 11, Page 1347
623 11, 1347 (2021).
- 624 36. Xu, Z., Guo, K., Chu, W., Lou, J. & Chen, C. Performance of Machine Learning
625 Algorithms for Predicting Adverse Outcomes in Community-Acquired Pneumonia.
626 *Front Bioeng Biotechnol* 10, 1 (2022).
- 627 37. El-Bouri, W. K., Sanders, A. & Lip, G. Y. H. Predicting acute and long-term mortality
628 in a cohort of pulmonary embolism patients using machine learning. *Eur J Intern Med*
629 (2023) doi:10.1016/J.EJIM.2023.07.012.
- 630 38. Beldi-Ferchiou, A. *et al.* High effector-memory CD8+ T-cell levels correlate with high
631 PML risk in natalizumab-treated patients. *Mult Scler Relat Disord* 46, 102470 (2020).
- 632 39. Dallari, S. *et al.* Upregulation of integrin expression on monocytes in multiple sclerosis
633 patients treated with natalizumab. *J Neuroimmunol* 287, 76–79 (2015).
- 634 40. Härzschel, A., Zucchetto, A., Gattei, V. & Hartmann, T. N. VLA-4 Expression and
635 Activation in B Cell Malignancies: Functional and Clinical Aspects. *Int J Mol Sci* 21,
636 (2020).
- 637 41. Roy, N. H. *et al.* LFA-1 signals to promote actin polymerization and upstream migration
638 in T cells. *J Cell Sci* 133, (2020).
- 639 42. Papayannopoulou, T., Priestley, G. V. & Nakamoto, B. Anti-VLA4/VCAM-1—Induced
640 Mobilization Requires Cooperative Signaling Through the kit/mkit Ligand Pathway.
641 *Blood* 91, 2231–2239 (1998).
- 642 43. Ley, K., Rivera-Nieves, J., Sandborn, W. J. & Shattil, S. Integrin-based therapeutics:
643 Biological basis, clinical use and new drugs. *Nature Reviews Drug Discovery* vol. 15
644 173–183 Preprint at <https://doi.org/10.1038/nrd.2015.10> (2016).
- 645 44. Dupré, L., Houmadi, R., Tang, C. & Rey-Barroso, J. T Lymphocyte Migration: An
646 Action Movie Starring the Actin and Associated Actors. *Front Immunol* 6, (2015).
- 647 45. Havrdova, E., Galetta, S., Stefoski, D. & Comi, G. Freedom from disease activity in
648 multiple sclerosis. *Neurology* 74 Suppl 3, (2010).
- 649 46. Pedregosa, F. *et al.* Scikit-learn: Machine Learning in Python. *Journal of Machine*
650 *Learning Research* 12, 2825–2830 (2011).

651

652 Acknowledgments

653 The authors thank Astrid Canivet and David Sagnat from the Organoïd facility of the Institut
654 de Recherche en Santé Digestive (IRSD). This work was supported by Brazilian Federal

655 Agency for Support and Evaluation of Graduate Education (CAPES, grant numbers CAPES-
656 PRINT - 88887.571313/2020-00) to B.C., and by research grants from the Brazilian Research
657 Council (CNPq) and the Rio de Janeiro Research Council (FAPERJ) to V.C.-d.-A, the São
658 Paulo State Research Foundation (FAPESP, grant numbers 2018/14933-2 to H.N.; 2019/27139-
659 5 to J.C.S.S.), the French MS society (ARSEP) to R.L. and B.C. and the French National Centre
660 for Scientific Research (CNRS, International Research Project SystAct to L.D.).

661

662 **Authorship information**

663 B.C. contributed to the design of the research, performed experiments, designed the analytical
664 pipeline, analyzed data and wrote the paper; J.S.S, H.N. and M.A. supervised analysis and built
665 the predictive models; F.B contributed to patient sample management and patient data
666 collection; C.L., G.P. and S.K. performed experiments; A.L.A, M.M. and J.S. participated in
667 scientific discussions; R.L participated in research design and scientific discussions; V.C.-d.-
668 A. and L.D. designed the research, supervised the analysis pipeline and wrote the paper.

669

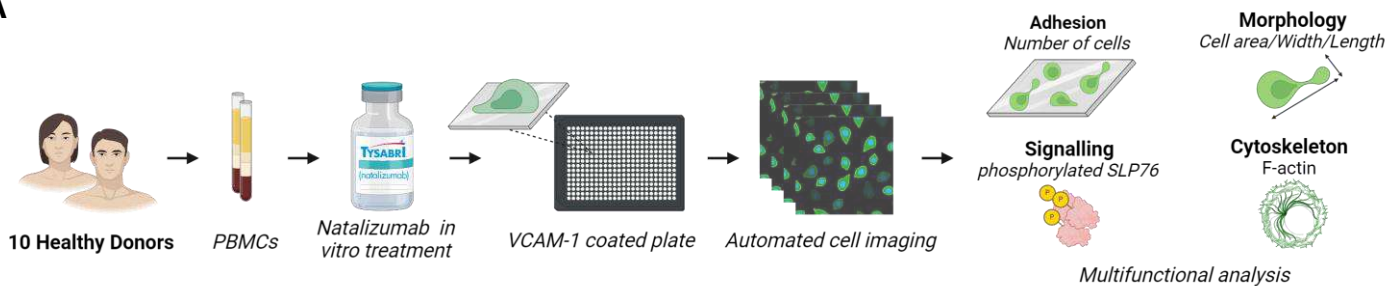
670 **Declaration of Interests**

671 The authors declare no competing interests.

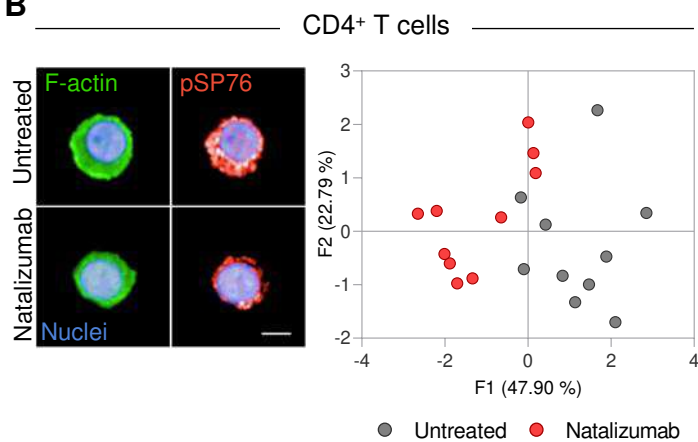
672

673

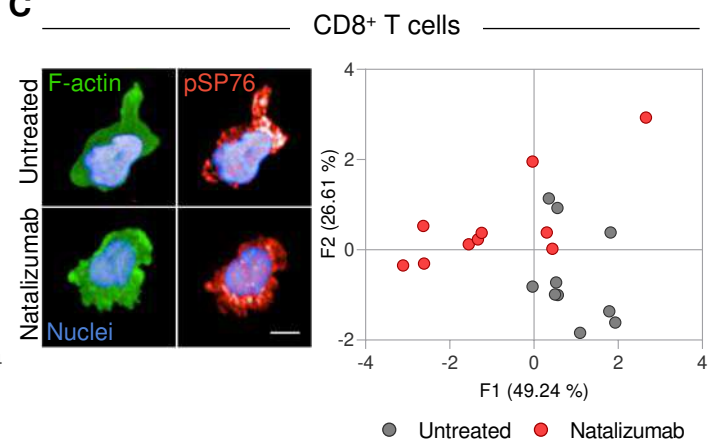
A



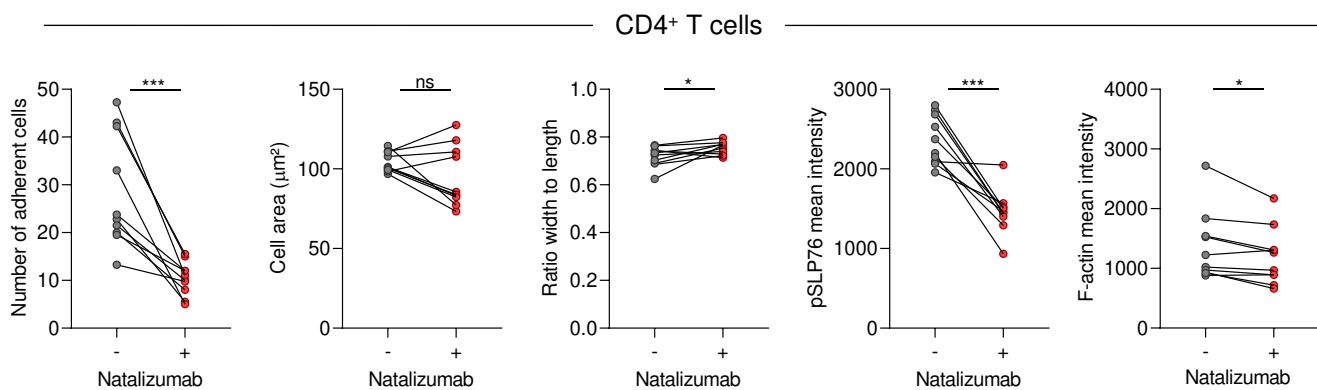
B



C



D



E

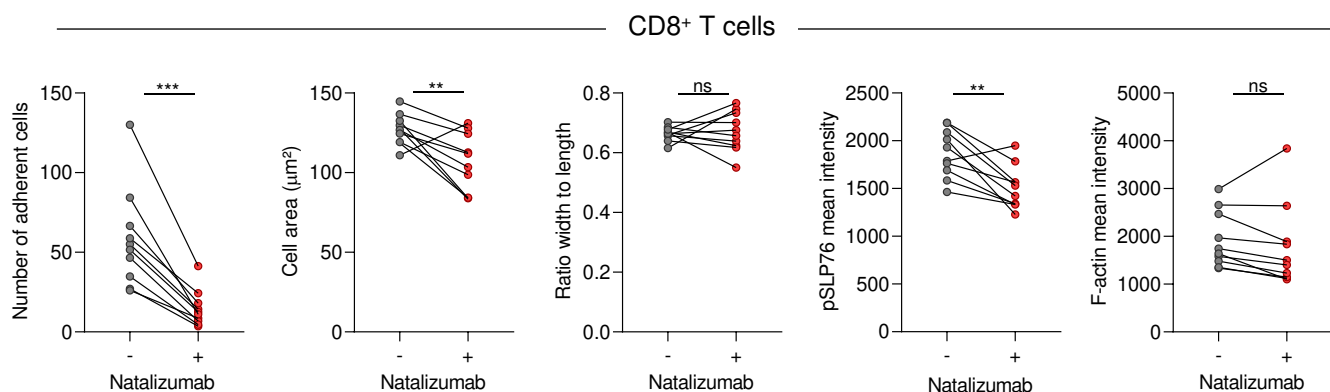


Figure 1. Automated cell imaging of healthy donor peripheral blood T cells upon *in vitro* natalizumab exposure

(A) Schematic of the HCI pipeline applied to PBMCs from healthy donors. PBMCs are exposed or not to natalizumab, seeded on VCAM-1 coated plates, stained for CD4 or CD8, F-actin and pSLP76 and imaged with an automated confocal microscope. Parameters pertaining to cell adhesion, cell shape, F-actin and pSLP76 are extracted separately from CD4⁺ and CD8⁺ subpopulations for further analysis.

(B and C) Representative 40x confocal images of CD4⁺ (B) and CD8⁺ (C) T cells, exposed or not to natalizumab, seeded on VCAM-1 and stained for F-actin (green), pSLP76 (red) and nuclei (blue). Scale bar: 5 μ m. PCA plots indicative of the effect of natalizumab on CD4⁺ (B) and CD8⁺ (C) T cells, based on parameters pertaining to adhesion, morphology, actin and pSLP76 intensity. Dots correspond to individual donors with data stemming from two independent experiments, each with 2 replicates.

(D and E) Values for individual parameters are shown for CD4⁺ T cells (D) and CD8⁺ T cells (E) in unexposed and natalizumab exposed samples. Parameters include number of adherent cells, cell area, width to length ratio, pSLP76 mean intensity and F-actin mean intensity. Dots correspond to individual donors with data stemming from two independent experiments, each with 2 replicates. Paired t test was used for statistical evaluation (ns = $p > 0.05$; * = $p \leq 0.05$; ** = $p \leq 0.01$ and *** = $p \leq 0.001$).

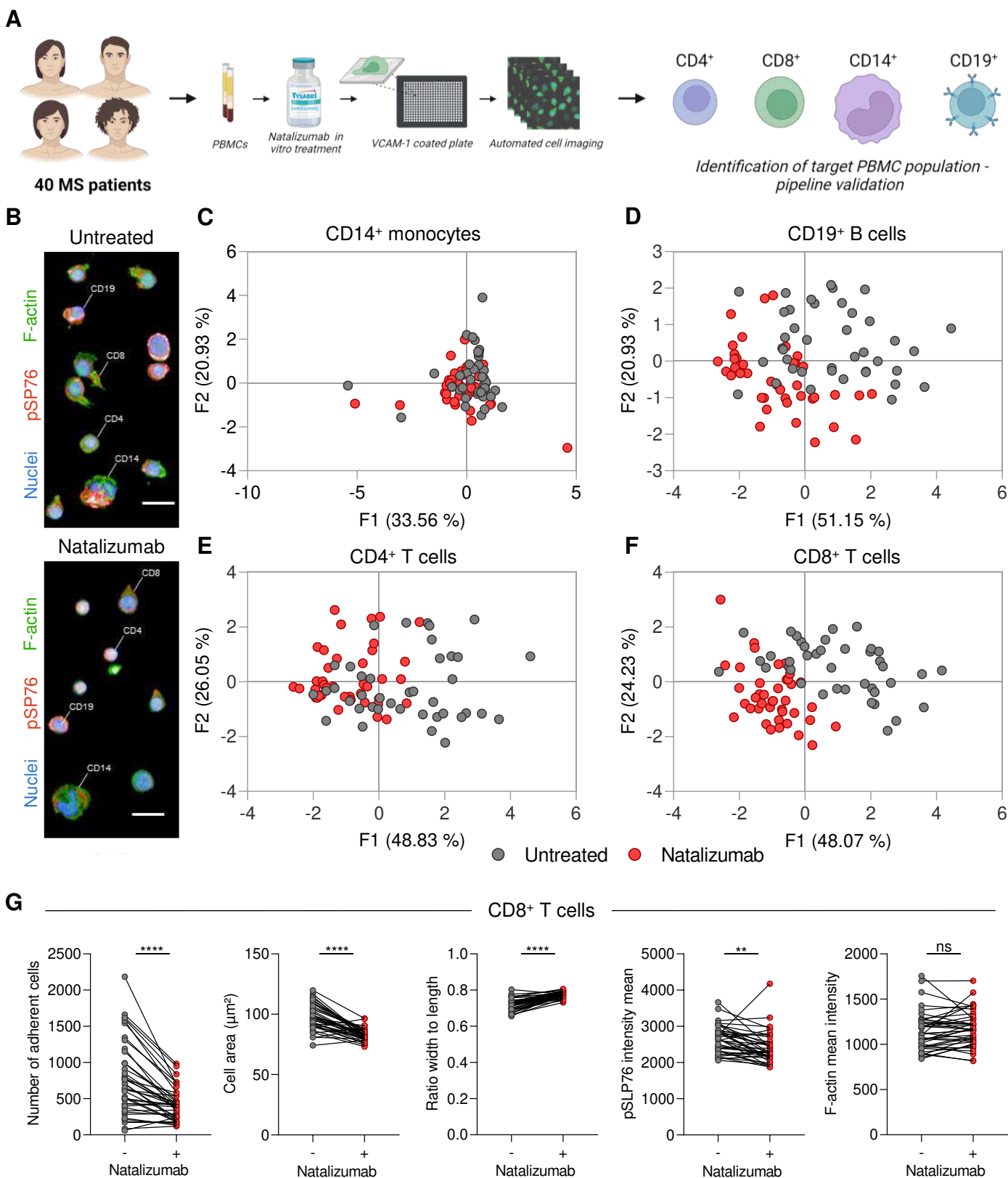


Figure 2. CD8⁺ T cells from MS patients display high sensitivity to natalizumab *in vitro* exposure

(A) Schematic of the HCI pipeline applied to pre-treatment PBMCs from MS patients. PBMCs are exposed or not to natalizumab, seeded on VCAM-1 coated plates, stained for CD4, CD8, CD14 or CD19, F-actin and pSLP76 and imaged with an automated confocal microscope. Parameters pertaining to cell adhesion, cell shape, F-actin and pSLP76 are extracted separately from CD4⁺, CD8⁺, CD14⁺ and CD19⁺ subpopulations for further analysis.

(B) Representative 20x confocal images of PBMCs from MS patients unexposed (top) or exposed to natalizumab (bottom), seeded on VCAM-1 and stained for F-actin (green), pSLP76 (red) and nuclei (blue). Scale bar: 20 μm . Individual CD4⁺ and CD8⁺ T cells, CD19⁺ B cells and CD14⁺ monocytes are indicated with a white line. Image does not represent cells from a same well.

(C-F) PCA plots indicative of the effect of natalizumab on CD14⁺ monocytes (C), CD19⁺ B cells (D), CD4⁺ T cells (E) and CD8⁺ T cells (F), based on parameters pertaining to adhesion, morphology, actin and pSLP76 intensity. Dots correspond to individual patients with data stemming from three independent experiments, each with 2 replicates.

(G) Values for individual parameters are shown for CD8⁺ T cells in unexposed and natalizumab exposed samples. Parameters include number of adherent cells, cell area, width to length ratio, pSLP76 mean intensity and F-actin mean intensity. Dots correspond to individual patients with data stemming from three independent experiments, each with 2 replicates. Paired t test was used for statistical evaluation (ns = $p > 0.05$; ** = $p \leq 0.01$ and **** = $p \leq 0.0001$).

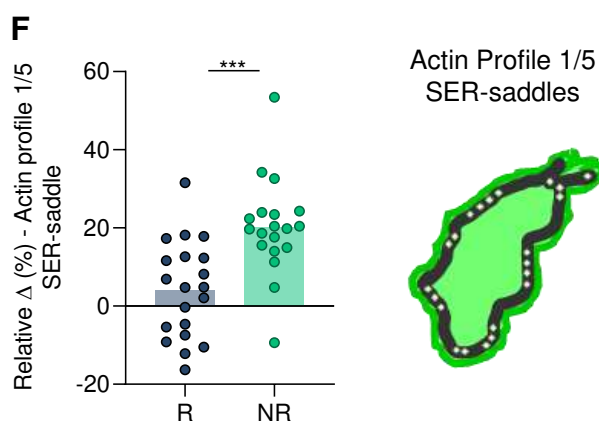
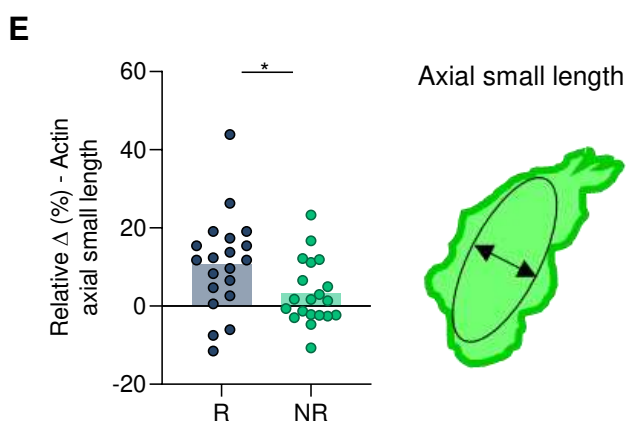
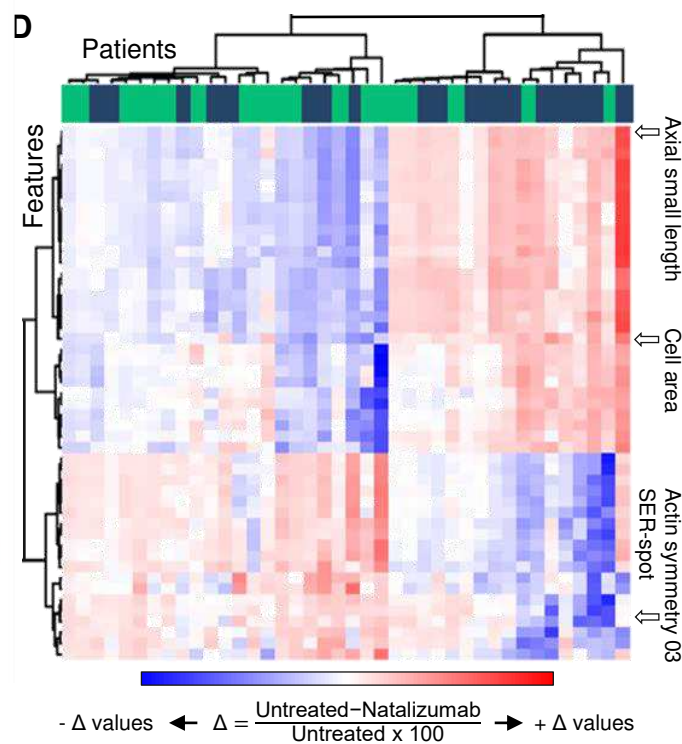
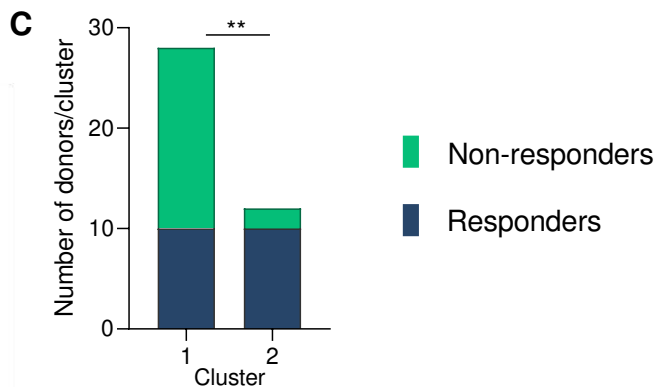
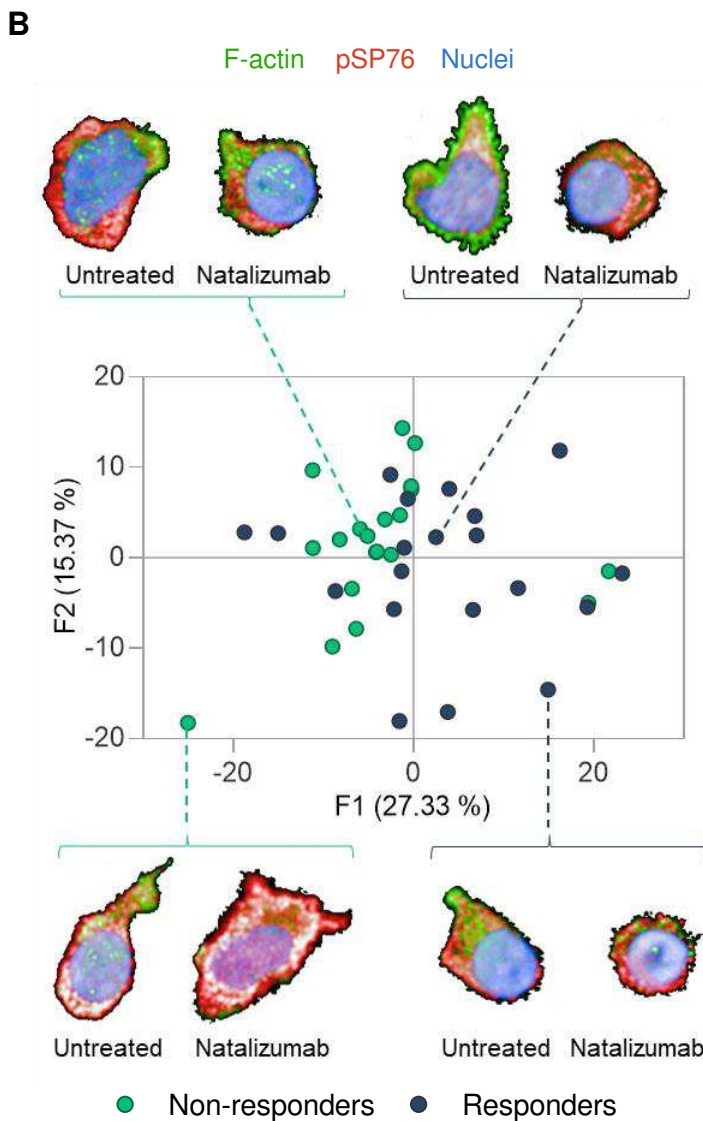
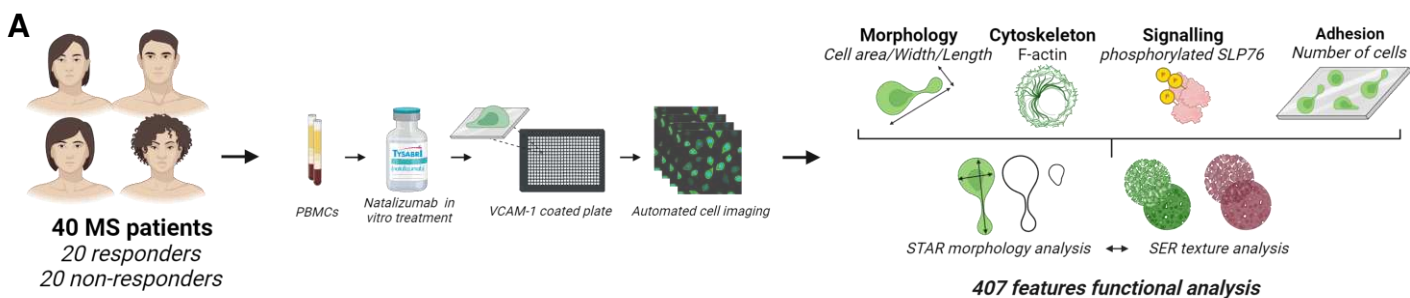


Figure 3. Automated cell imaging discriminates CD8⁺ T cells according to natalizumab treatment outcome in MS patients

(A) Schematic of the HCI pipeline applied to pre-treatment PBMCs from MS patients and aiming at identifying morphological signatures associated with natalizumab treatment outcome. PBMCs are exposed or not to natalizumab, seeded on VCAM-1 coated plates, stained for CD8, F-actin and pSLP76 and imaged at high resolution with an automated confocal microscope. A total of 407 parameters are extracted from each imaged CD8⁺ T cell for further analysis.

(B) Representative 63x confocal images of CD8⁺ T cells from 4 MS patients exposed or not to natalizumab, seeded on VCAM-1 and stained for F-actin (green), pSLP76 (red) and nuclei (blue). Scale bar (brackets): 45 μ m. PCA plot aggregating the data from 407 features pertaining to cell adhesion, morphology, F-actin and pSLP76 intensity, distribution and texture (Harmony STAR morphology and SER texture features). Each feature was analyzed as a normalized delta value ((untreated sample – natalizumab-treated sample) / natalizumab-treated \times 100)) to account for the effect of natalizumab. Each dot represents a single MS patient with data stemming from three independent experiments. Clinical response to natalizumab treatment is indicated by the dot color.

(C) K-means clustering analysis of the entire HCI dataset, yielding two clusters that partially segregate responder (blue) or non-responder patients (green). A Chi-square test was used for statistical evaluation (** = $p \leq 0.01$).

(D) Ward clustering analysis of the HCI dataset represented as heatmap with dendrogram. The analysis was restricted to the 50 top features along F1 component of the PCA. The upper dendrogram represents the clustering of the 40 patients, indicating partial segregation of responder (blue) or non-responder patients (green). The left dendrogram represents the clustering of the 50 features, according to the intensity and the direction of the effect of natalizumab exposure (blue: natalizumab exposure increases the value of the considered feature; red: natalizumab exposure reduces the value of the considered feature).

(E-F) Relative delta values are shown for Actin axial small length (E) and Actin profile 1/5 SER-saddle (F), two features exemplifying the distinct *in vitro* effect of natalizumab on CD8⁺ T cells from responder (blue dots) and non-responder patients (green dots). Bars represent the mean of the considered patient subgroup. An unpaired t-test was used for statistical evaluation (* = $p \leq 0.05$; *** = $p \leq 0.001$). Schematics of Actin axial small length and Actin profile 1/5 SER-saddle are represented on the side of the corresponding graphs.

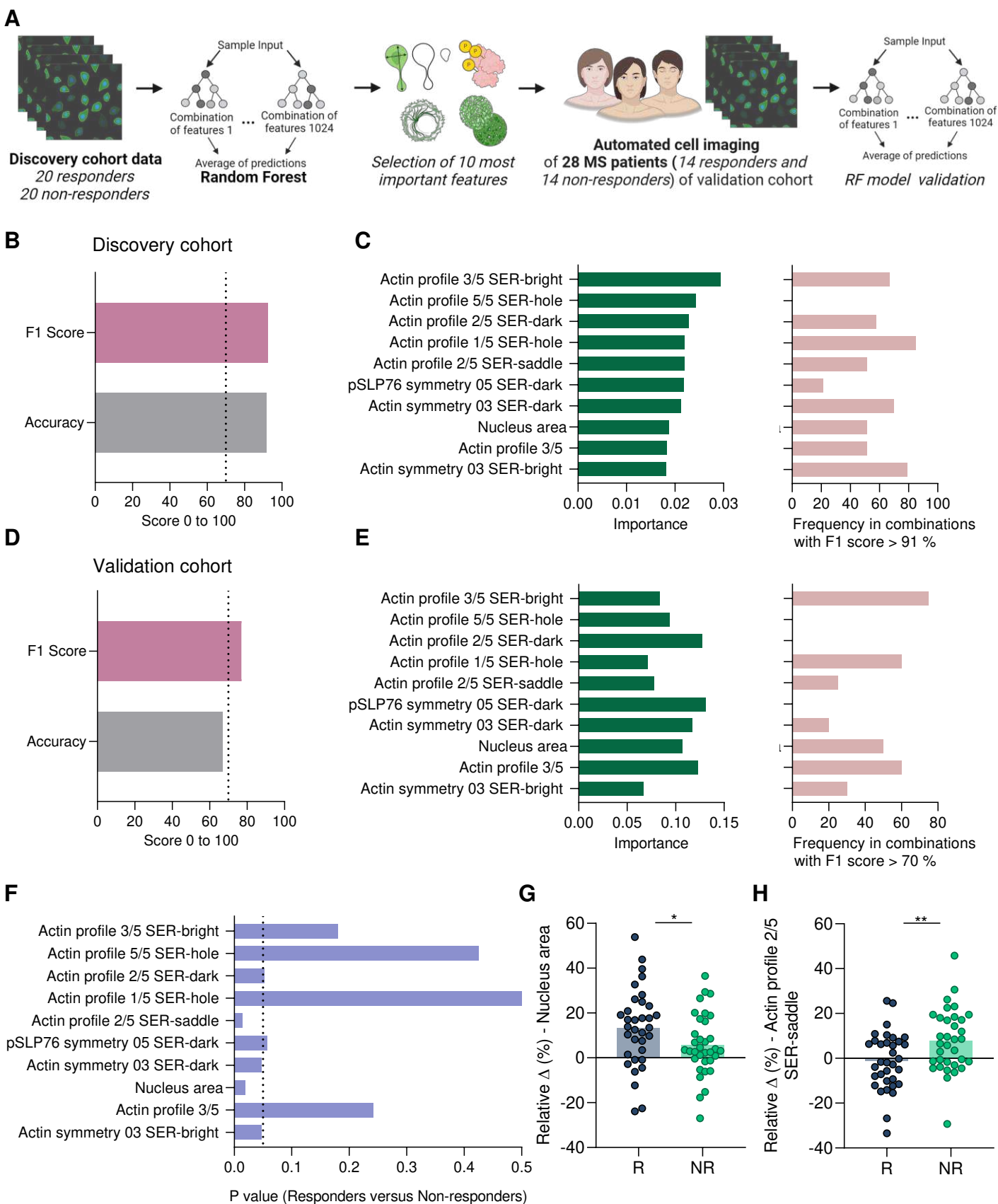


Figure 4. Random Forest approach predicts natalizumab treatment outcome in MS patients

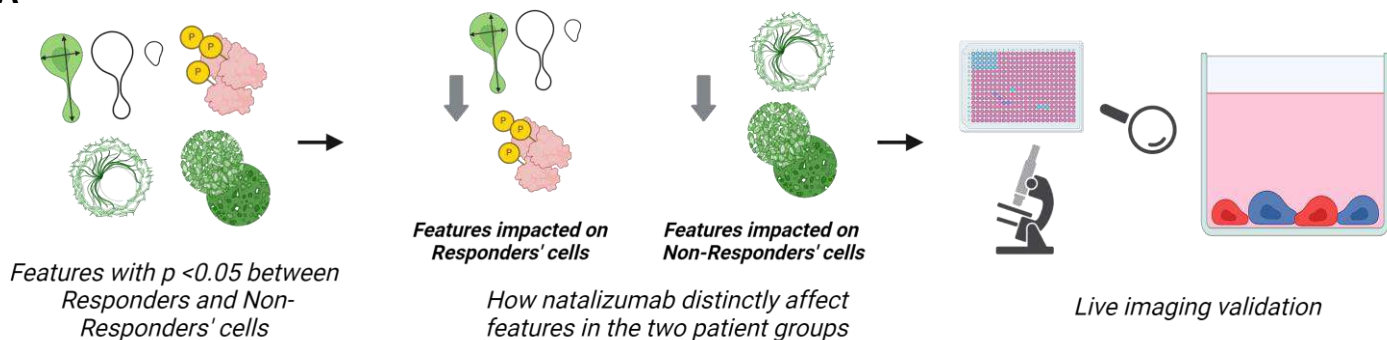
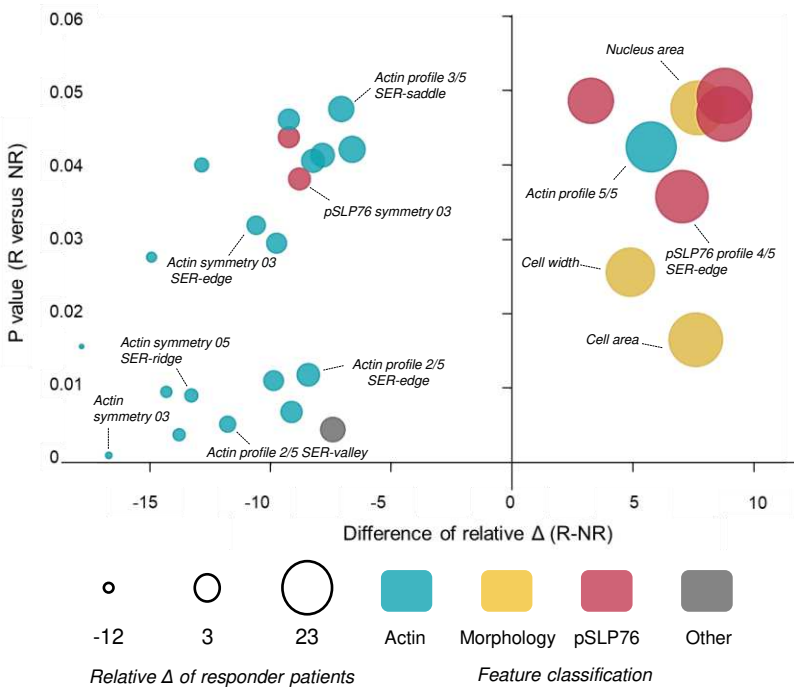
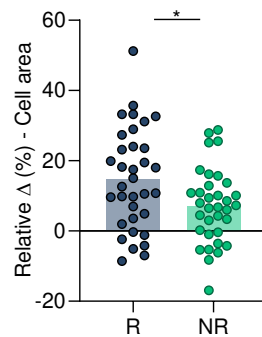
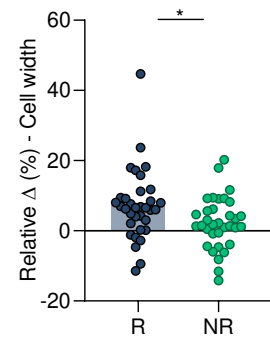
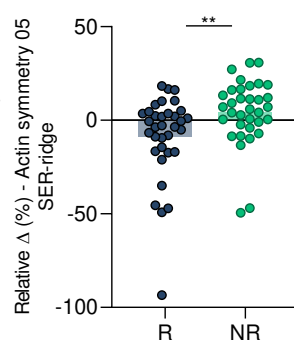
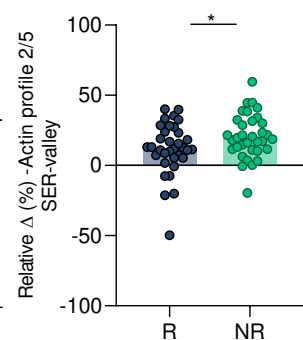
(A) Schematic of the machine learning approach build to predict response to natalizumab treatment on the basis of the analysis of pretreatment PBMC with the HCI pipeline. A RF model is trained on the HCI dataset from a discovery cohort composed of 20 responder and 20 non-responder patients. The elaborated model, which runs with 1024 combinations of a restricted set of 10 features, is then challenged with the HCI dataset from a validation cohort composed of 14 responder and 14 non-responder patients.

(B and D) Highest accuracy and F1-score obtained among 1024 combinations of features applied to decision-tree constructions performed in the RF model. (B) represents RF performance with the discovery cohort (40 MS patients), calculated with 133 features. (D) represents RF performance with the validation cohort (28 MS patients), calculated with the 10 most important features identified in the discovery cohort. Dashed line represents wished threshold of 70% for both scores.

(C and E) Importance of each individual feature and feature frequency on RF combinations with F1 score > 91 % in the RF approach for the discovery cohort (C), importance and frequency on RF combinations with F1 score > 70% for the validation cohort (E).

(F) P values of unpaired t-tests calculated for each of the 10 most important features between the group of responder versus non-responder patients from both cohorts merged (n=68, 34 patients in each subgroup).

(G and H) Relative delta values are shown for Nucleus area (G) and Actin Profile 2/5 SER-saddle (H), two prominent features of the RF model. The relative delta values represent the in vitro effect of natalizumab on CD8+ T cells from responder (blue dots) and non-responder patients (green dots). Bars represent the mean of the considered patient subgroup. An unpaired t-test was used for statistical evaluation (* = $p \leq 0.05$; ** = $p \leq 0.01$).

A**B****C****D****E****F****G**

Untreated

Natalizumab

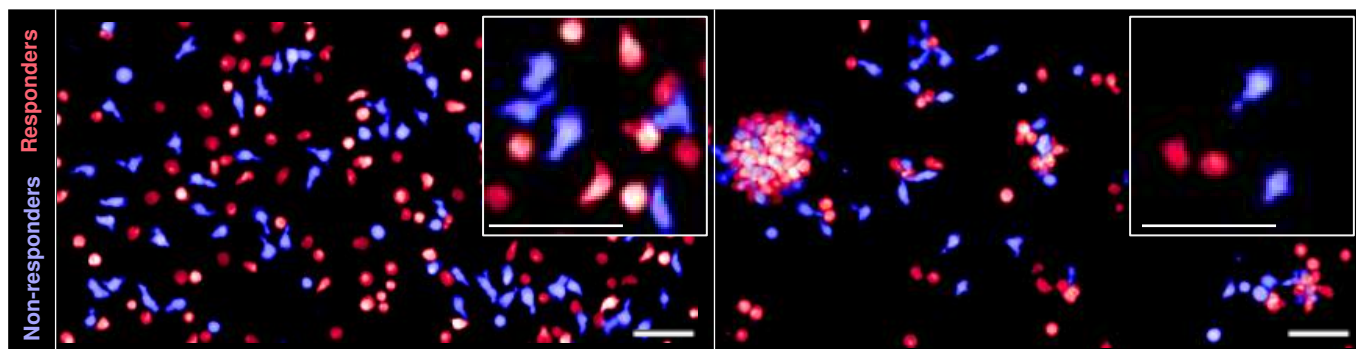
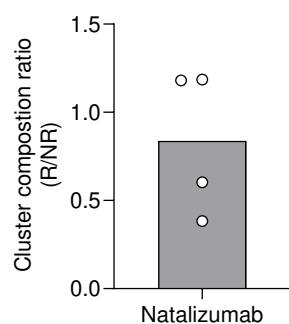
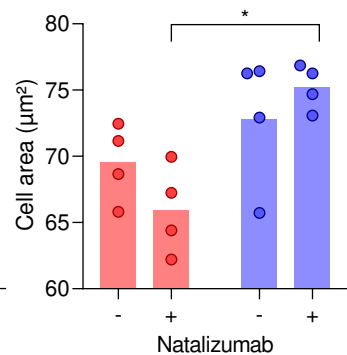
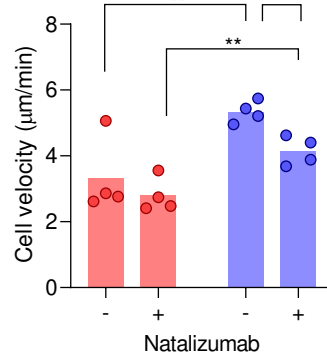
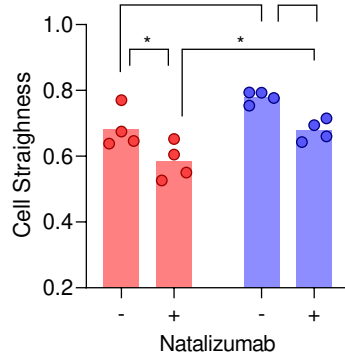
**H****I****J****K**

Figure 5. CD8⁺ T cells from non-responder patients are resistant to natalizumab inhibition of cell spreading

(A) Schematic of the identification of discriminatory features to natalizumab clinical outcomes based on HCI Imaging pipeline and RF analyzes.

(B) Combined analysis of the 29 features with distinct behavior for the responder versus non-responder patients (n=68), based on a p value <0.05 (unpaired t-tests). The Y axis of the chart represents the calculated p value. The X-axis of the chart represents the difference of relative delta mean (Δ responder – Δ non-responder). The size of the bubbles represents the delta average of each feature in the responder patient subgroup, as indicated in the legend. The color of the bubbles represents feature categories, as indicated in the legend.

(C-F) Cell area (C), cell width (D), Actin symmetry 05 SER-ridge (E) and Actin profile 2/5 SER-valley (F) based on the average relative delta of CD8⁺T cells from responder and non-responder MS patients exposed or not *in vitro* to natalizumab. Data represent the mean of 3 HCI experiments conducted on 68 MS patients. Bars represent the mean of the considered patient subgroup. Unpaired t-tests were used for statistical evaluation (* = $p \leq 0.05$, ** = $p \leq 0.01$).

(G) Representative snap shots of migrating CD8⁺ T cells from one responder and one non-responder MS patient under agarose at the presence or VCAM-1. Blue indicates non-responders' cells and red indicates responders' cells. Scale bars represent 40 μ m. At the right of each image, representative zoom of cells *in vitro* treated or not with natalizumab.

(H) Ratio of responder/non-responder cells per homotypic aggregation cluster. Bar represents the average of 4 responders' cells and 4 non-responders treated with natalizumab cells after 1h of migration.

(I) Cell area of migrating CD8⁺ T cells from 4 responder MS patients and 4 non-responder MS patients *in vitro* treated or not with natalizumab, under agarose and over VCAM-1. Data were obtained from 301 to 3085 cells per condition and are representative of 3 independent experiments. Bar represents the cell area average of 4 responders' cells and 4 non-responders' cells after 1h of migration. Sidak's multiple comparisons test was used for statistical evaluation (* = $p \leq 0.05$).

(J and K) Mean speed (J) and cell straightness (K) of migrating CD8⁺ T cells from 4 responders MS patients and 4 non-responders MS patients under agarose over VCAM-1. Data were obtained from 301 to 3085 cells per condition and are representative of 3 independent experiments. Bar represents the cell speed average of 4 responders' cells and 4 non-responders' cells along 2h tracks. Sidak's multiple comparisons test was used for statistical evaluation (** = $p \leq 0.01$).

Supplementary Files

This is a list of supplementary files associated with this preprint. Click to download.

- [ChavesSupplMaterials submission20240605NatComms.pdf](#)